DEPARTMENT OF PHYSICS

ATMOSPHERIC, OCEANIC AND PLANETARY PHYSICS

QUAGMIRE: QUAsi-Geostrophic Model for Investigating Rotating fluids Experiments

Reference Manual for Version 1.2

P. D. Williams
Centre for Global Atmospheric Modelling, Department of Meteorology, University of Reading, UK

T. W. N. Haine
Department of Earth and Planetary Sciences, Johns Hopkins University, USA

P. L. Read, S. R. Lewis, Y. H. Yamazaki
Atmospheric, Oceanic, and Planetary Physics, Clarendon Laboratory, University of Oxford, UK

AOPP Technical Memorandum 2004.3

10 June 2004

University of Oxford

Foreword

QUAGMIRE is a quasi-geostrophic numerical model, intended for carrying out fast, high-resolution simulations of multi-layer rotating annulus laboratory experiments on a desktop PC.

The model uses a hybrid finite-difference/spectral approach to numerically integrate the coupled nonlinear partial differential equations of motion in cylindrical geometry in each layer. The flow is forced by a differentially rotating annulus lid. The effects of weak interfacial tension are included, as well as the quadratic (centripetal) beta-effect. The annulus base and lid are both allowed to have a constant radial slope, giving a topographic beta-effect. Dissipation is achieved through Ekman layer pumping/suction at the horizontal boundaries, including the internal interface(s). A leapfrog time stepping scheme is used, with a Robert filter. An optional stochastic forcing module is included, to represent the effects of unresolved features.

At the present time, the model is written for the special case of two layers of equal resting depths, but there are plans to generalize this in the future.

When simulating a laboratory experiment at reasonably high resolution, on a 1.4 GHz desktop PC, the model can run up to ten times faster than "real life". The run time memory requirement is 3 MB. The model waves, which grow due to baroclinic instability if the Froude number is supercritical, have phase speeds, equilibrated amplitudes and wavenumbers which agree well with laboratory experiments. For Froude numbers which are higher still, more complicated model flows result, such as amplitude vacillations with reasonable amplitudes and periods and, ultimately, flow which is highly irregular and appears to be chaotic.

A tar file, containing the model source code, a makefile, a shell script and a Matlab diagnostics suite, can be obtained by e-mailing the authors:

P. D. Williams (williams@atm.ox.ac.uk) NCAS Centre for Global Atmospheric Modelling, Department of Meteorology, University of Reading, PO Box 243, Earley Gate, Reading, RG6 6BB, UK

T. W. N. Haine (thomas.haine@jhu.edu) Department of Earth and Planetary Sciences, 329 Olin Hall, 34th and North Charles Streets, Johns Hopkins University, Baltimore, Maryland 21218, USA

P. L. Read (read@atm.ox.ac.uk) Atmospheric, Oceanic and Planetary Physics, Clarendon Laboratory, Parks Road, Oxford, OX1 3PU, UK

S. R. Lewis (lewis@atm.ox.ac.uk) Atmospheric, Oceanic and Planetary Physics, Clarendon Laboratory, Parks Road, Oxford, OX1 3PU, UK

Y. H. Yamazaki (hiro@atm.ox.ac.uk) Atmospheric, Oceanic and Planetary Physics, Clarendon Laboratory, Parks Road, Oxford, OX1 3PU, UK

Contents

1 Introduction **2**
1.1 Overview 2
1.2 Dynamical similarity and laboratory experiments 2
1.3 Primitive versus filtered models . . . 3
1.4 Review of filtered models 4
1.4.1 Candidate filtered model types 4
1.4.2 Candidate geometries 4

2 Continuous model equations **6**
2.1 Derivation of the model equations . 6
2.1.1 Perturbation equations 8
2.2 Normal mode decomposition of diagnostic equations 9
2.3 Perturbation streamfunction boundary conditions for the continuous equations 10
2.3.1 Integral properties of the prognostic equations 11
2.3.2 Integral properties of the diagnostic equations 11

3 Discretization of the equations **14**
3.1 The model grid 14
3.2 Prognostic equations 14
3.2.1 Azimuthal derivative 14
3.2.2 Jacobian 15
3.2.3 Laplacian 15
3.3 Diagnostic equations 15
3.4 Perturbation streamfunction boundary conditions for the discretized equations 16
3.5 Details of the numerical schemes . . 16
3.5.1 Time stepping 16
3.5.2 Time-lagged diffusion 17
3.5.3 Hyperdiffusion 17
3.5.4 Stochastic parameterization of sub-gridscale effects 17
3.6 Summary of numerical integration scheme 18
3.7 Initial conditions 19

4 Technical model details **20**
4.1 Model source code 20
4.2 Tests of the model code 21
4.3 Namelist 21
4.4 Shell script 22
4.5 Suitable values for the numerical parameters 22
4.6 Matlab diagnostics 23

5 Closing remarks **25**
5.1 Summary 25
5.2 Future plans 25

1 Introduction

1.1 Overview

For over a century, geophysicists have invoked the principle of fluid dynamical similarity to make possible the study of geofluids (planetary atmospheres, oceans and liquid cores) in the laboratory. The main benefits of studying geofluids indirectly in this way are that the system is under the complete control of the experimenter, that global high-resolution measurements can be systematically taken, and that experiments can be repeated as many times as required. None of these statements hold when such flows are studied directly rather than in the laboratory. Indeed, it seems clear that we should not want to perform experiments on the real atmosphere and ocean, for fear of what the consequences might be if the experiment goes wrong! A review of the role of laboratory experiments in geophysical fluid dynamics has been given by Hide (1977).

The advent of computer models for studying the general circulation of atmospheres and oceans, was accompanied by the development of corresponding models for simulating the fluid flows in rotating laboratory experiments. Such experiments are always simplified analogues of the geophysical systems which they are intended to mimic, so that the focus of the study can be restricted to a small number of well-defined phenomena in isolation. Because of their relative simplicity, laboratory flows are generally easier to reliably numerically model than geoflows. The comparison between laboratory and model flows therefore remains an important testbed for investigating many fundamental dynamical phenomena.

In this manual, we describe the design and construction of a new numerical model for simulating fluid flows in discrete-layer rotating annulus laboratory experiments. We review a variety of candidate model types in the remainder of this section, each with different dynamical assumptions, and choose to construct a quasi-geostrophic model. A model with a full representation of the annular geometry is preferable to a Cartesian channel model, for a number of important reasons which are discussed.

The two-layer quasi-geostrophic coupled partial differential equations in cylindrical coordinates are derived in Section 2, and the diagnostic relations between streamfunction and potential vorticity are decomposed into vertical and azimuthal normal mode form to simplify their solution. Suitable sidewall boundary conditions are derived by considering integral properties of the governing equations. Then, the continuous equations are carefully discretized in Section 3, in such a way as to preserve discrete analogues of the integral properties. Suitable initial conditions are given. In Section 4, the calculations are partitioned into model subroutines, and the technical details of how to run the model are described. Suitable numerical parameter values and initial conditions are given, and the model code units are tested to ensure that they are free from errors. Future plans for the model are discussed in Section 5.

The model has become known as QUAGMIRE, the *QUAsi-Geostrophic Model for Investigating Rotating fluids Experiments*.

1.2 Dynamical similarity and laboratory experiments

It is well-known (Douglas & Gasiorek, 2000) that, when written in non-dimensional form, the equations which govern the evolution of seemingly different fluid dynamical systems can be very similar. The aim of laboratory experiments in geophysical fluid dynamics is to exploit this *dynamical similarity*, to make inferences about atmospheric, oceanic and liquid core phenomena from observations of the analogous laboratory flows.

For example, the quasi-geostrophic equations for an approximated two-layer atmosphere or ocean, can very closely resemble those for a rotating, two-layer laboratory experiment. This statement holds despite the fact that typical length and time scales for corresponding geophysical and laboratory flows can differ by very many orders of magnitude. All that matters for dynamical similarity is equality of the relevant *non-dimensional* dynamical and geometrical parameters, such as the Rossby number and aspect ratio.

Dynamical similarity allows us to study geofluids in the laboratory, as suggested by Figure 1. Once we have solved a particular fluid flow problem by making observations in the laboratory, we have actually solved an infinite number of other fluid flow problems all of which are dynamically and geo-

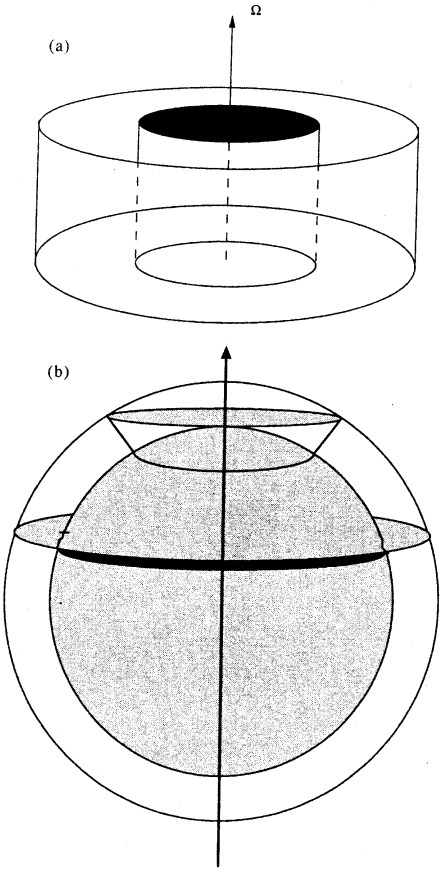

Figure 1: Diagram showing the analogy between (a) the fluid in a rotating annulus experiment in the laboratory, and (b) the fluid bounded by two latitude circles on a rotating planet. From Read et al. (1998).

metrically similar, including on the planetary scale.

Laboratory investigations of non-rotating fluid flows began in the nineteenth century, and include the classic investigations of Reynolds (1883). At around the same time, Vettin (1884) was probably the first to exploit dynamical similarity by carrying out rotating laboratory experiments as analogues of geophysical systems. He studied the surface flow in a rotating dishpan of fluid with a lump of ice near the centre, representing a polar ice cap, and (to the scorn of his contemporaries) he drew meteorological conclusions from his results.

As suggested by Vettin's experiment, for the closest resemblance between the annulus and planet in Figure 1, we should apply heating and cooling at the outer and inner vertical sidewalls, respectively, to mimic the differential solar thermal forcing between equator and pole. The resulting *rotating thermal annulus* system with continuous fluid stratification has been extensively studied since the early 1950s, including the classic experiments of Hide et al. (1977).

It follows from the thermal (and gradient) wind balance equations for a rapidly-rotating annulus, that a radial temperature gradient will be accompanied by a vertical shear in the zonal velocity (such as that associated with the tropospheric jetstream in the atmosphere). Flows which are mathematically similar to those obtained in the thermal annulus, can therefore be obtained in an isothermal annulus by imposing a velocity shear directly. For studying geoflows, an alternative to the thermal annulus is therefore the *rotating two-layer annulus*, with a shear provided across the fluid interface by differentially-rotating top and bottom horizontal boundaries. The rotating, two layer annulus has also been studied extensively in the laboratory (e.g. Carrigan, 1978; King, 1979; Appleby, 1982; Lovegrove, 1997; Williams, 2003), and is the subject of the present numerical model.

1.3 Primitive versus filtered models

One possible numerical approach would be a direct numerical simulation (DNS) of the Navier-Stokes or shallow water equations, both of which are referred to as primitive equation sets, because only relatively minor approximations are made, and so both vortical and divergent eigenmodes are retained. DNS codes have been developed

for the continuously-stratified, rotating thermal annulus (e.g. Hignett et al., 1985; White, 1986) but these would require significant modification in order to be applicable to a discrete-layer, isothermal system. Furthermore, DNS codes are very computationally expensive, and could be used to examine not more than a few case studies at reasonably high resolution.

As an alternative to a DNS for the present numerical simulations, we choose to use a balanced model, in which small-scale, divergent modes are filtered out by construction. Because of the filtering of unbalanced modes, balanced models have fewer dynamical degrees of freedom than DNS models, and therefore run much more quickly, allowing larger numbers of simulations to be performed. Such filtering is justified because the interaction between vortical and divergent modes is conventionally thought to be negligible.

1.4 Review of filtered models

The relative merits of three candidate filtered model types and two candidate geometries are now discussed.

1.4.1 Candidate filtered model types

Three commonly-used filtered models for simulating rapidly-rotating, two-layer flows are those based on the *quasi-geostrophic equations*, the *balance equations* and the *slow equations*. These three equation sets can each be derived from the *shallow water equations*, which in turn are derived from the *Navier-Stokes equations* under the assumptions of hydrostatic balance and columnar flow. Discussions of these and other filtered models are given by McWilliams & Gent (1980) and by McIntyre & Norton (2000).

The main assumptions made in the derivation of the quasi-geostrophic equations, first used by Charney et al. (1950), are that the potential vorticity is advected only by the geostrophic component of the flow, and that the amplitudes of perturbations to the fluid surfaces are much smaller than the mean fluid depths.

The balance equations (Charney, 1955) are derived by performing a horizontal velocity decomposition into vortical and divergent components, and then truncating with respect to the divergent component. The balance that they describe is more complicated, but also more accurate, than geostrophic balance, and efficient procedures have been developed to integrate them (Daley, 1982). However, it has been pointed out by Moura (1976) that, in their most general form, the balance equations have spurious non-physical wave solutions with phase speeds much larger than those of inertia-gravity waves.

The slow equations (Lynch, 1989) are derived in a similar way to the balance equations, except that the velocity truncation is performed in a more systematic manner (based on normal mode initialization) which results in the vanishing of the spurious solutions. Numerical integrations of the slow equations show excellent agreement with initialized numerical integrations of the shallow water equations.

Of these three candidate models, we choose the quasi-geostrophic (Q-G) equations for the present numerical model. This is because only one scalar function of horizontal position is needed per layer to uniquely define the state of the system using a Q-G model (i.e. streamfunction), whereas three are needed per layer using a balance or slow equations model (i.e. streamfunction, velocity potential and geopotential). With three times fewer independent variables, the computational advantages gained from using a Q-G model were felt to outweigh the disadvantages of its slightly lower formal accuracy.

1.4.2 Candidate geometries

A number of numerical Q-G models have been developed for systems consisting of superposed immiscible fluid layers in a rectangular channel (e.g. Brugge et al., 1987). For the following reasons, however, it was decided that none of these Cartesian models could meet the present requirements.

Firstly, the channel equations with periodic azimuthal boundary conditions are a good approximation to the annulus equations only if the ratio of the width of the annular gap to its mean radius is much smaller than unity (King, 1979). With this geometry, the curvature becomes negligible, and we would be justified in using a channel model to simulate the flow in an annulus. For typical

laboratory annulus experiments, though, this ratio is usually around 6 cm/9 cm, or 0.7, which is only slightly smaller than 1.

Secondly, channel models have additional, shift-reflect symmetries (Cattaneo & Hart, 1990) not present in annulus models. This is the case because, though the annulus and periodic channel are topologically similar, the geometry of their boundaries is fundamentally different. For example, there is a reflect symmetry in the channel in the plane which is equidistant from the sidewall boundaries, but there is no analogous symmetry in the annulus. Kwon & Mak (1988) show that the existence of such additional symmetries in the periodic channel leads to certain vortical wave-wave interaction coefficients being identically zero. Importantly, an annular model would allow the complete set of wave-wave interactions that take place in the laboratory experiments, to be included in the model, which is important for quantitative agreement.

Furthermore, a model in cylindrical coordinates would be more general, and potentially applicable to laboratory experiments other than annuli. For example, it would keep open the possibility of running simulations in an open cylinder with no inner sidewall, as well as in an annulus, though it would then be necessary to include an inner sidewall of small nominal radius in the model, to avoid the singularity at $r = 0$. We would need to assume that the flow is insensitive to the inclusion of this additional boundary.

There are background potential vorticity gradients present in both the channel and the annulus, due to the sloping of equilibrium geopotential height surfaces in the presence of a vertical shear in horizontal velocity. In the channel, these geopotential height and potential vorticity variations are linear in the across-channel direction (equivalent to a β-effect), whereas in the annulus they are quadratic because of the parabolic equilibrium interface height shape produced by centripetal effects. This gives an effective *quadratic β-effect*, with the possibility of qualitatively different dynamics than in the presence of the usual linear β-effect.

As a final point, not connected with geometry, few of the existing Q-G layer channel models include the effects of interfacial tension, which can be significant in the laboratory.

Since we desire quantitative agreement with laboratory experiments, we conclude that we need to construct a new multi-layer Q-G model which takes into account the cylindrical geometry, centripetal effects and interfacial tension. Such a model is described in the remainder of this manual.

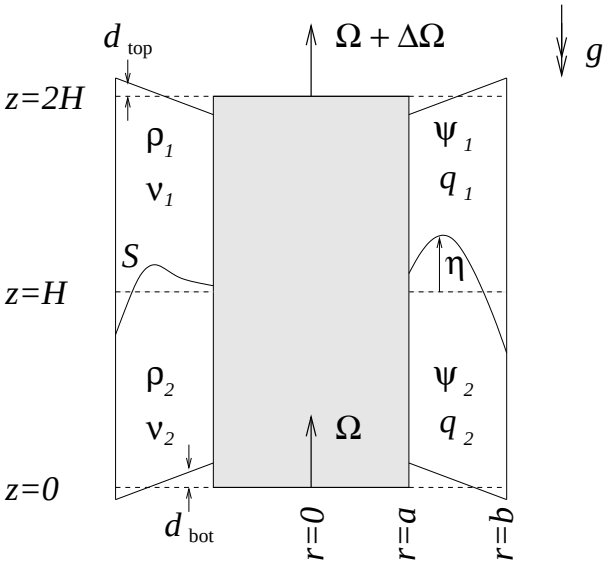

Figure 2: Schematic diagram showing a vertical cross-section through the two-layer annulus system being modelled. The dashed line shows the resting interface height. See text for definitions.

2 Continuous model equations

2.1 Derivation of the model equations

The system to be modelled is shown schematically in Figure 2. Such a model is often informally referred to as two-and-a-half dimensional, as the representation of the vertical dimension is achieved through only two discrete layers. Cylindrical polar coordinates $\boldsymbol{r} = (r, \theta, z)$ are used, the z-axis being coincident with the vertical rotation axis. The fluid is bounded by a base of mean vertical position $z = 0$, a lid of mean vertical position $z = 2H > 0$ and cylindrical walls at $r = a$ and $r = b > a$. The base and lid linearly deviate from their mean vertical positions by $d_{\rm bot}(r)$ and $d_{\rm top}(r)$, respectively, and we define the constants $s_{\rm bot} = {\rm d}d_{\rm bot}/{\rm d}r$ and $s_{\rm top} = {\rm d}d_{\rm top}/{\rm d}r$. The two homogeneous, immiscible layers have constant densities ρ_i, kinematic viscosities ν_i and mutual interfacial tension S, where we use the oceanography convention that $i = 1$ refers to the upper layer, and $i = 2$ to the lower layer. The undisturbed fluid interface has vertical position $z = H$, and the disturbed fluid interface has vertical position $z = H + \eta(\boldsymbol{r}, t)$. The acceleration due to gravity is g. The annulus base and walls rotate about the axis of symmetry with angular velocity Ω, and the lid with angular velocity $\Omega + \Delta\Omega$.

Working in a frame which rotates with the base, the four fundamental equations for the pressure $p_i(\boldsymbol{r}, t)$ and the velocity $\boldsymbol{u}_i(\boldsymbol{r}, t)$ in layer i are the Navier-Stokes equations:

$$\frac{\partial \boldsymbol{u}_i}{\partial t} + (\boldsymbol{u}_i \cdot \boldsymbol{\nabla})\boldsymbol{u}_i + 2\boldsymbol{\Omega} \times \boldsymbol{u}_i + \boldsymbol{\Omega} \times (\boldsymbol{\Omega} \times \boldsymbol{r}) = -\frac{1}{\rho_i}\boldsymbol{\nabla} p_i + \nu_i \nabla^2 \boldsymbol{u}_i + \boldsymbol{g} \quad (1)$$

and the equation of volume conservation for the incompressible liquid:

$$\boldsymbol{\nabla} \cdot \boldsymbol{u}_i = 0 \ . \quad (2)$$

We take the curl of equation (1) and use vector identities to obtain an equation for the layer vorticities $\boldsymbol{\omega}_i = \boldsymbol{\nabla} \times \boldsymbol{u}_i$:

$$\frac{\partial \boldsymbol{\omega}_i}{\partial t} + (\boldsymbol{u}_i \cdot \boldsymbol{\nabla})\boldsymbol{\omega}_i = [(2\boldsymbol{\Omega} + \boldsymbol{\omega}_i) \cdot \boldsymbol{\nabla}]\boldsymbol{u}_i + \nu_i \nabla^2 \boldsymbol{\omega}_i \ , \quad (3)$$

the z-component of which, in the layer interiors where the flow is assumed to be vertically-columnar and inviscid, is

$$\frac{\partial \xi_i}{\partial t} + (\boldsymbol{u}_i \cdot \boldsymbol{\nabla})\xi_i = (f + \xi_i)\frac{\partial u_{i,\,z}}{\partial z} \ , \quad (4)$$

where ξ_i is the z-component of $\boldsymbol{\omega}_i$, $f = 2\Omega$ is the Coriolis parameter and $u_{i,\,z}$ is the vertical velocity.

We next vertically integrate equation (4) over the fluid interiors, parameterizing vertical Ekman pumping/suction velocities (Gill, 1982) at the lid, base and interface, which are all assumed to have small slopes. Assuming that the Ekman layer depths are much smaller than the total layer depths, and making the quasi-geostrophic assumptions $\eta, d_{\rm bot}, d_{\rm top} \ll H$ and $\xi_i \ll f$, we obtain, after rearrangement:

$$\left(\frac{\partial}{\partial t} + \boldsymbol{u}_1 \cdot \boldsymbol{\nabla}\right) q_1 = -\frac{\sqrt{\Omega\nu_1}}{H}\left[\xi_1 + \chi_2(\xi_1 - \xi_2)\right] + 2\Delta\Omega\frac{\sqrt{\Omega\nu_1}}{H} \ , \quad (5)$$

$$\left(\frac{\partial}{\partial t} + \boldsymbol{u}_2 \cdot \boldsymbol{\nabla}\right) q_2 = -\frac{\sqrt{\Omega\nu_2}}{H}\left[\xi_2 + \chi_1(\xi_2 - \xi_1)\right] \ , \quad (6)$$

where $\chi_i = \sqrt{\nu_i}/(\sqrt{\nu_1} + \sqrt{\nu_2})$, and $q_i(r, \theta, t)/H$ are the perturbation potential vorticities (PPVs), given by

$$q_1(r, \theta, t) = \xi_1 + \frac{f(\eta - d_{\rm top})}{H} \quad (7)$$

and

$$q_2(r,\theta,t) = \xi_2 - \frac{f(\eta - d_{\rm bot})}{H} \ . \qquad (8)$$

To complete the derivation, we write all of the independent variables ($\boldsymbol{u}_i$, ξ_i and η) in equations (5)–(8) in terms of the layer streamfunctions $\psi_i(r,\theta,t)$ defined by

$$u_{i,\,\theta} = \frac{\partial \psi_i}{\partial r} \qquad (9)$$

and

$$u_{i,\,r} = -\frac{1}{r}\frac{\partial \psi_i}{\partial \theta} \ . \qquad (10)$$

The streamfunctions ψ_1 and ψ_2 are defined only to within arbitrary additive constants, which will be discussed in Section 2.3.2. The vorticities are given by

$$\xi_i = \nabla^2 \psi_i \ . \qquad (11)$$

Assuming hydrostatic balance and nearly equal layer densities, the interface height perturbation is given in terms of the streamfunctions (to within an additive constant) by

$$\eta - \delta_m^2 \nabla^2 \eta = \frac{f}{g'}(\psi_2 - \psi_1) + \frac{r^2\Omega^2}{2g} \ , \qquad (12)$$

where $g' = 2g(\rho_2 - \rho_1)/(\rho_2 + \rho_1)$ is the reduced gravity. The term in $\delta_m = \sqrt{S/[g(\rho_2 - \rho_1)]}$ represents the effects of interfacial tension for an interface of small curvature. δ_m is the characteristic static meniscus width, as can be seen by considering solutions to equation (12) when the tank is at rest ($\Omega = 0$) and the fluid velocities are zero (ψ_i = constant). The full equation (12) is a forced Helmholtz equation for η given ψ_i, where the boundary conditions are the slopes $\partial\eta/\partial r$ at the annulus walls, which are related to the interface contact angle. We require an explicit formula for η, and so we seek a first order solution to the Helmholtz equation for weak interfacial tension, by estimating the $\nabla^2\eta$ term in equation (12) using the solution for η when $\delta_m = 0$. This gives

$$\eta = \frac{f}{g'}(1 + \delta_m^2\nabla^2)(\psi_2 - \psi_1) + \frac{r^2\Omega^2}{2g} \ , \qquad (13)$$

where 1 and $\delta_m^2\nabla^2$ are the first two terms in a power series solution. On simple grounds, the series would be expected to converge rapidly if $\delta_m^2\nabla^2\eta \ll \eta$, which is the case if $\delta_m^2 \ll \lambda^2$ for waves of wavelength λ. We expect waves to form on the scale of the internal Rossby radius $\sqrt{g'H}/|f|$, and so the convergence criterion becomes $\delta_m^2 f^2/g'H \ll 1$. This is equivalent to $FI \ll 1$ where $F = f^2(b-a)^2/g'H$ is the Froude number and the non-dimensional parameter $I = \delta_m^2/(b-a)^2$ is the interfacial tension number (Appleby, 1982).

We finally substitute equations (9), (10), (11) and (13) into (5) and (6) to obtain the two coupled partial differential equations governing the evolution of quasi-geostrophic motions in the two-layer annulus:

$$\left(\frac{\rm D}{{\rm D}t}\right)_1 q_1 = -\frac{\sqrt{\Omega\nu_1}}{H}\left[\nabla^2\psi_1 + \chi_2\nabla^2(\psi_1 - \psi_2)\right] + \frac{2\Delta\Omega\sqrt{\Omega\nu_1}}{H} \qquad (14)$$

and

$$\left(\frac{\rm D}{{\rm D}t}\right)_2 q_2 = -\frac{\sqrt{\Omega\nu_2}}{H}\left[\nabla^2\psi_2 + \chi_1\nabla^2(\psi_2 - \psi_1)\right] \ . \qquad (15)$$

The total derivative operators are given by

$$\left(\frac{\rm D}{{\rm D}t}\right)_i = \frac{\partial}{\partial t} - \frac{1}{r}\frac{\partial\psi_i}{\partial\theta}\frac{\partial}{\partial r} + \frac{1}{r}\frac{\partial\psi_i}{\partial r}\frac{\partial}{\partial\theta} \qquad (16)$$

and the horizontal Laplacian operator is given by

$$\nabla^2 = \frac{\partial^2}{\partial r^2} + \frac{1}{r}\frac{\partial}{\partial r} + \frac{1}{r^2}\frac{\partial^2}{\partial\theta^2} \ . \qquad (17)$$

By substituting equations (11) and (13) into equations (7) and (8), we find that the quantities q_1 and q_2 are given in terms of ψ_1 and ψ_2 by

$$q_1 = \nabla^2\psi_1 + \frac{f^2}{g'H}(1 + \delta_{\rm m}^2\nabla^2)(\psi_2 - \psi_1) + \frac{f}{H}\frac{r^2\Omega^2}{2g} - \frac{f d_{\rm top}}{H} \qquad (18)$$

and

$$q_2 = \nabla^2\psi_2 - \frac{f^2}{g'H}(1 + \delta_{\rm m}^2\nabla^2)(\psi_2 - \psi_1) - \frac{f}{H}\frac{r^2\Omega^2}{2g} + \frac{f d_{\rm bot}}{H} \ . \qquad (19)$$

On the right side of equation (14), the first term represents spin-up/down by the frictional Ekman layers at the lid ($\nabla^2\psi_1$) and interface ($\nabla^2(\psi_1 - \psi_2)$). The second term is the (constant) forcing term, and represents generation of potential vorticity by the rotating lid, communicated to the fluid interior by an Ekman layer. The terms on

the right side of (15) have a similar interpretation, except that there is no explicit forcing term in this case.

Equations (18) and (19) are similar to the potential vorticity/streamfunction relationships in the channel model of Brugge et al. (1987), except that the present equations include an interfacial tension modification, and Brugge's βy term has been replaced with our $\beta^* r^2$ term. This is the quadratic β-effect. It is equal and opposite in the upper and lower layers, corresponding to the fact that depth increases in one layer are accompanied by equal decreases in the other layer.

Upon non-dimensionalization of equations (14), (15), (18) and (19), using a time scale $(\Delta\Omega)^{-1}$ and horizontal length scale $(b-a)$, definitions of Froude number, dissipation parameter, Rossby number, Reynolds number, Ekman number and interfacial tension number appear naturally. We choose to code the model using dimensional units, however, and therefore do not carry out the non-dimensionalization here.

We now summarize the assumptions which were required to derive equations (14)–(19). It is important to bear these approximations in mind, since they limit the applicability of the model:

- incompressible fluids
- vertically-columnar fluid interiors
- inviscid fluid interiors (i.e. Reynolds number $\mathrm{Re} \gg 1$)
- linear Ekman pumping/suction
- $\eta \ll H$, $d_{\mathrm{bot}} \ll H$, $d_{\mathrm{top}} \ll H$
- $|\boldsymbol{\nabla}\eta \ll 1|$, $|s_{\mathrm{bot}}| \ll 1$, $|s_{\mathrm{top}}| \ll 1$
- Ekman layer depths $\ll H$
- $\xi_i \ll f$ (i.e. Rossby number $\ll 1$)
- hydrostatic balance (i.e. $\mathrm{D}u_z/\mathrm{D}t \ll g$)
- $g' \ll g$
- $FI \ll 1$
- passive Stewartson layers which do not exchange fluid with the interiors
- Stewartson layer widths $\ll b-a$

The final two assumptions are discussed in Section 2.3, but are included here for completeness.

2.1.1 Perturbation equations

There is an equilibrium solution to equations (14)–(19) of the form $u_{i,\,r} = 0$, $u_{i,\,\theta} = r\Delta\Omega_i$. Substituting allows us to determine the interior solid-body rotation rates:

$$\frac{\Delta\Omega_1}{\Delta\Omega} = \frac{2+\chi}{2(1+\chi)} \tag{20}$$

and

$$\frac{\Delta\Omega_2}{\Delta\Omega} = \frac{1}{2(1+\chi)}\ , \tag{21}$$

where $\chi = \sqrt{\nu_2/\nu_1}$. The corresponding interface height (to within an additive constant) is given by equation (13) to be

$$\overline{\eta} = \frac{\Omega^2 r^2}{2g}\left(1 - \frac{\Delta\Omega/\Omega}{g'/g}\right)\ . \tag{22}$$

Equations (20)–(22) describe the basic, equilibrium state upon which baroclinically-unstable perturbations may grow. We refer to this as the *mean flow* and label the corresponding streamfunctions and PPVs as $\overline{\psi_i}(r)$ and $\overline{q_i}(r)$, respectively.

Governing equations for perturbations $\psi_i'(r,\theta,t)$ and $q_i'(r,\theta,t)$ to the streamfunctions and PPVs, respectively, are obtained by substituting $\psi_i = \overline{\psi_i}(r) + \psi_i'(r,\theta,t)$ and $q_i = \overline{q_i}(r) + q_i'(r,\theta,t)$ into equations (14)–(19) to obtain

$$\begin{aligned}\left(\frac{\mathrm{D}}{\mathrm{D}t}\right)_{1'} q_1' \;=\; & -\frac{\sqrt{\Omega\nu_1}}{H}\left[\nabla^2\psi_1' + \chi_2\nabla^2(\psi_1'-\psi_2')\right] \\ & -\Delta\Omega_1\frac{\partial q_1'}{\partial\theta} \\ & +\frac{f^2}{2H}\left(\frac{\Omega}{g}-\frac{\Delta\Omega}{g'}\right)\frac{\partial\psi_1'}{\partial\theta} \\ & -\frac{f s_{\mathrm{top}}}{rH}\frac{\partial\psi_1'}{\partial\theta}\end{aligned} \tag{23}$$

and

$$\begin{aligned}\left(\frac{\mathrm{D}}{\mathrm{D}t}\right)_{2'} q_2' \;=\; & -\frac{\sqrt{\Omega\nu_2}}{H}\left[\nabla^2\psi_2' + \chi_1\nabla^2(\psi_2'-\psi_1')\right] \\ & -\Delta\Omega_2\frac{\partial q_2'}{\partial\theta} \\ & -\frac{f^2}{2H}\left(\frac{\Omega}{g}-\frac{\Delta\Omega}{g'}\right)\frac{\partial\psi_2'}{\partial\theta} \\ & +\frac{f s_{\mathrm{bot}}}{rH}\frac{\partial\psi_2'}{\partial\theta}\ ,\end{aligned} \tag{24}$$

where

$$q_1' = \nabla^2\psi_1' + \frac{f^2}{g'H}(1+\delta_{\mathrm{m}}^2\nabla^2)(\psi_2'-\psi_1') \tag{25}$$

and

$$q'_2 = \nabla^2\psi'_2 - \frac{f^2}{g'H}(1+\delta_{\rm m}^2\nabla^2)(\psi'_2-\psi'_1)\ . \quad (26)$$

The total derivatives in equations (23) and (24) now advect according to the perturbation streamfunctions, i.e.

$$\left(\frac{\rm D}{{\rm D}t}\right)_{i'} = \frac{\partial}{\partial t} - \frac{1}{r}\frac{\partial\psi'_i}{\partial\theta}\frac{\partial}{\partial r} + \frac{1}{r}\frac{\partial\psi'_i}{\partial r}\frac{\partial}{\partial\theta} \quad (27)$$
$$\equiv \frac{\partial}{\partial t} + J(\psi'_i,*)\ .$$

Equations (23)–(26) are the nonlinear model equations which we solve. The constant forcing term in equation (14), which represents forcing of the full flow by the lid rotation, has been replaced in equations (23) and (24) with more complicated non-constant forcing terms which represent forcing of the perturbation flow by the equilibrium state and the bottom and top topography. An analytical assessment of the stability of small perturbations could begin by linearizing equations (23) and (24), i.e. discarding the advection terms, but for the model we retain all of the nonlinear terms.

The perturbation velocity fields are given in terms of the perturbation streamfunctions by

$$u'_{i,\,\theta} = \frac{\partial\psi'_i}{\partial r} \quad (28)$$

and

$$u'_{i,\,r} = -\frac{1}{r}\frac{\partial\psi'_i}{\partial\theta}\ , \quad (29)$$

which are the perturbation forms of equations (9) and (10). The perturbation interface height field is given (to within an additive constant) by

$$\eta' = \frac{f}{g'}(1+\delta_m^2\nabla^2)(\psi'_2-\psi'_1)\ , \quad (30)$$

which is the perturbation form of equation (13).

2.2 Normal mode decomposition of diagnostic equations

Given the fields ψ'_i and q'_i at any time, we can evaluate $\partial q'_i/\partial t$ at that time using the prognostic equations (23) and (24). There are contributions to the PPV tendency from the advection ($J(\psi'_i,q'_i)$), forcing ($\partial/\partial\theta$) and dissipation (∇^2) terms. We can thereby determine q'_i at a short time in the future. We may then use this to invert the diagnostic Helmholtz equations (25) and (26) to obtain ψ'_i at that time, and then begin the loop again using the updated fields. This is how QUAGMIRE integrates the model equations.

The Helmholtz equations (25) and (26) are coupled, and the inversion is made easier by first writing them in vertical normal mode form to remove the coupling. We take the sum and difference of the equations to obtain, respectively,

$$\nabla^2(\psi'_1+\psi'_2) = q'_1+q'_2 \quad (31)$$

and

$$\nabla^2(\psi'_2-\psi'_1) - C_{\rm itcc}\frac{2f^2}{g'H}(\psi'_2-\psi'_1) = C_{\rm itcc}(q'_2-q'_1)\ , \quad (32)$$

where $C_{\rm itcc}$ is an interfacial tension correction coefficient given by

$$C_{\rm itcc} = \frac{1}{1-(2f^2\delta_m^2)/(g'H)}\ . \quad (33)$$

We know that $f^2\delta_m^2/g'H \ll 1$ (Section 2.1), and so $C_{\rm itcc}$ is slightly larger than unity, and is exactly equal to unity if the interfacial tension is zero.

Defining the barotropic (bt) and baroclinic (bc) vertical normal mode variables to be

$$\Psi'_{\rm bt} = \psi'_1+\psi'_2\ , \quad (34)$$
$$\Psi'_{\rm bc} = \psi'_2-\psi'_1\ , \quad (35)$$
$$Q'_{\rm bt} = q'_1+q'_2\ , \quad (36)$$
$$Q'_{\rm bc} = C_{\rm itcc}(q'_2-q'_1)\ , \quad (37)$$

equations (31) and (32) both become uncoupled Helmholtz equations of the form

$$\nabla^2\Psi'_m - \lambda_m\Psi'_m = Q'_m \quad (38)$$

for $m = {\rm bt}, {\rm bc}$. The eigenvalues are $\lambda_{\rm bt} = 0$ and $\lambda_{\rm bc} = 2C_{\rm itcc}f^2/g'H$.

We now perform a second normal mode decomposition, this time into azimuthal modes, to further simplify the solution of the Helmholtz equations. At each timestep, we expand

$$\Psi'_m(r,\theta) = \sum_{n=-\infty}^{\infty}\hat{\Psi}'^n_m(r)e^{\sqrt{-1}n\theta}\ , \quad (39)$$

$$Q'_m(r,\theta) = \sum_{n=-\infty}^{\infty}\hat{Q}'^n_m(r)e^{\sqrt{-1}n\theta}\ . \quad (40)$$

The complex functions $\hat{\Psi}'^n_m$ and $\hat{Q}'^n_m$ satisfy $\hat{\Psi}'^n_m = \hat{\Psi}'^{-n^*}_m$ and $\hat{Q}'^n_m = \hat{Q}'^{-n^*}_m$, where the asterisk represents complex conjugation, because $\Psi'_m(r,\theta)$ and

$Q'_m(r,\theta)$ are real. The $n = 0$ term is called the *mean flow correction* (a correction to the zonal flow that is generated by nonlinear self interactions of the waves), and is equal to the zonal average of the perturbation quantities as can be seen from the zonal integration of equations (39) and (40). The $n \neq 0$ terms represent eddy (wave) components. Substituting equations (39) and (40) into (38) gives the radial structure equation:

$$\frac{\mathrm{d}^2\hat{\Psi}'^n_m}{\mathrm{d}r^2} + \frac{1}{r}\frac{\mathrm{d}\hat{\Psi}'^n_m}{\mathrm{d}r} - \left(\lambda_m + \frac{n^2}{r^2}\right)\hat{\Psi}'^n_m = \hat{Q}'^n_m(r) \ . \tag{41}$$

This complex ordinary differential equation must be solved for each combination of vertical modes $m \in \{\mathrm{bt}, \mathrm{bc}\}$ and azimuthal modes $n \in \{0, \pm1, \pm2, \ldots\}$ to determine $\hat{\Psi}'^n_m(r)$ given $\hat{Q}'^n_m(r)$. The inversion process required to obtain $\psi'_i(r,\theta)$ from $q'_i(r,\theta)$, which are linked by equations (25) and (26), is therefore summarized as:

$$\begin{array}{ccccc} q'_i & \xrightarrow{(36)\,\&\,(37)} & Q'_{\mathrm{m}} & \xrightarrow{(40)} & \hat{Q}'^n_m \\ & & & & \downarrow (41) \\ \psi'_i & \xleftarrow{(34)\,\&\,(35)} & \Psi'_{\mathrm{m}} & \xleftarrow{(39)} & \hat{\Psi}'^n_m \end{array}$$

We could now perform a third normal mode decomposition, this time in the radial coordinate, by projecting $\hat{\Psi}'^n_m(r)$ and $\hat{Q}'^n_m(r)$ onto the eigenfunctions of the linear operator on the left side of equation (41). The baroclinic eigenfunctions are *modified Bessel functions* of order n in the scaled radial coordinate $\tilde{r} = \sqrt{\lambda_{\mathrm{bc}}}\, r$ (Boas, 1983), and the barotropic eigenfunctions are of the form $r^{\pm n}$. However, this approach would force the streamfunction and PPV to satisfy the same boundary conditions, for which there is no justification. In the present model, we therefore solve the discretized radial structure equation directly rather than projecting onto radial modes.

2.3 Perturbation streamfunction boundary conditions for the continuous equations

We must now choose boundary conditions to apply to the perturbation streamfunction when integrating equation (41). The equation was derived under the assumption of inviscid flow. It therefore cannot describe the thin, viscous Stewartson layers of width δ_S which exist at the lateral boundaries, and so applies only to the fluid interior $a + \delta_S < r < b - \delta_S$. We assume that $\delta_S \ll a, b$ so that we may still write the integration range as $a < r < b$, but from now on when we refer to $r = a$ or $r = b$ we mean the boundary between the fluid interior and Stewartson layer, rather than the physical lateral boundary itself.[1]

There are a number of candidate boundary conditions. To impose passive Stewartson layers which do not anywhere exchange fluid with the interior, we would apply the impermeability condition to the radial perturbation velocity $u'_{i,\,r}|_{r=a,\,b} = 0, \quad \forall\, \theta, i$, which in the normal mode variables corresponds to Dirichlet boundary conditions

$$\hat{\Psi}'^n_m|_{r=a,\,b} = 0 \quad \forall\, n \neq 0, m \ . \tag{42}$$

The mean flow correction velocity ($n = 0$) is purely zonal, and so this component automatically satisfies impermeability. Impermeability alone is therefore not a sufficient condition to uniquely specify a solution. No-slip boundary conditions for the zonal perturbation velocity $u'_{i,\,\theta}|_{r=a,\,b} = 0, \quad \forall\, \theta, i$, correspond in the normal mode variables to the Neumann conditions

$$\left.\frac{\mathrm{d}\hat{\Psi}'^n_m}{\mathrm{d}r}\right|_{r=a,\,b} = 0 \quad \forall\, n, m \ . \tag{43}$$

The equilibrium solid-body rotation flow about which we perturb satisfies impermeability, but is not no-slip.

Since we are solving a second order differential equation, only two independent boundary conditions are required. We cannot therefore impose both impermeable and no-slip flow at both boundaries, as that would require four independent conditions. This over-constrained nature of the PPV inversion in Q-G models has been discussed by Williams (1979). A comprehensive study of the comparative effects of using no-slip boundary conditions, rather than the more traditional free-slip conditions, is described by Mundt et al. (1995).

We are therefore forced to use a reduced set of boundary conditions, but we must choose carefully and consistently which conditions to retain and

[1] An alternative method for keeping the Stewartson layers out of the analysis would be to imagine that our laboratory apparatus is equivalent to a *gedanken* experiment in which, at all times in each layer, the lateral boundaries rotate at the same rate as the fluid interiors, so that the Stewartson layers vanish.

which to abandon, to avoid any possibility of non-physical behaviour. We are, of course, free to employ different boundary conditions for the different normal mode components specified by m and n.

The debate over suitable lateral Q-G boundary conditions has had a long and contentious history in the literature. In the classic periodic channel models of Phillips (1954) and Phillips (1956), boundary conditions corresponding to equation (42) are used for the wave ($n \neq 0$) terms, and equation (43) is used for the mean flow correction ($n = 0$) component only. The latter condition was not imposed (but the former was retained) in the studies of Phillips (1963) and Pedlosky (1964), but McIntyre (1967) showed that relaxing this mean flow correction boundary condition leads to a spurious, unspecified energy flux through the sidewalls. The condition was included again in Pedlosky (1970), but replaced in Pedlosky (1971) and Pedlosky (1972) with an *ad-hoc* condition chosen for mathematical convenience. Smith (1974) points out that the resulting non-physical energy source might well invalidate Pedlosky's results, and repeats Pedlosky's calculations with the proper boundary condition retained (Smith & Pedlosky, 1975; Smith, 1977). More recent studies (Appleby, 1982; Yoshida & Hart, 1986; Lewis, 1992; Stephen, 1998) have avoided the spurious energy and associated unreliable conclusions by applying both conditions in full, as in Phillips' original paper.

An informative interpretation of Phillips' mean flow correction boundary condition has been given by Davey (1978). For non-zero zonal perturbation velocities $u'_{i,\,\theta}|_{r=a,\,b}$ at the boundary between the interior and a Stewartson layer, there will be a corresponding return volume flux between the Ekman layers and the Stewartson layer due to the asymmetry of the Ekman spiral (Pedlosky, 1987), which will have a non-zero radial component proportional to $u'_{i,\,\theta}|_{r=a,\,b}$. We can therefore ensure that there is no net build-up of mass in the Stewartson layers by setting

$$\int_0^{2\pi} u'_{i,\,\theta}|_{r=a,\,b}\,\mathrm{d}\theta = 0 \quad \forall\, i\ . \tag{44}$$

This condition is automatically satisfied for the wave $n \neq 0$ components, and is equivalent to equation (43) with $n = 0$, which is the condition used by Phillips. With this condition, there is no *net* exchange of fluid due to the perturbation flow between each Ekman layer and the Stewartson layers, though *local* exchange is allowed.

Next, we derive a consistent and plausible set of boundary conditions for the annulus, which do not lead to non-physical behaviour, by considering integral properties of both the prognostic and diagnostic model equations.

2.3.1 Integral properties of the prognostic equations

Consider the area-integral of the perturbation PPV tendencies over the annular domain:

$$\int_{\theta=0}^{2\pi}\int_{r=a}^{b} \frac{\partial q'_i}{\partial t}\, r\,\mathrm{d}r\,\mathrm{d}\theta\ , \tag{45}$$

as given by the prognostic equations (23) and (24). The linear $\partial/\partial\theta$ forcing terms integrate to give zero unconditionally. The advection terms in the total derivatives integrate to give zero (Salmon & Talley, 1989) if

$$\left.\frac{\partial \psi'_i}{\partial \theta}\right|_{r=a,\,b} = 0\ , \tag{46}$$

and the dissipation (∇^2) terms integrate to give zero if

$$\int_0^{2\pi} \left.\frac{\partial \psi'_i}{\partial r}\right|_{r=a,\,b} \mathrm{d}\theta = 0\ . \tag{47}$$

The two conditions (46) and (47) are equivalent to impermeability for the waves and no-slip for the mean flow correction, as originally used by Phillips. With these conditions, the mean layer PPVs are conserved by the continuous equations and there is no spurious energy flux. We choose to apply these conditions to the present model, except that the latter condition leads to an ill-posed PPV inversion for the special case $n = 0$, $m = \mathrm{bt}$, as we will now see.

2.3.2 Integral properties of the diagnostic equations

Equation (41) for the barotropic mean flow correction is

$$\frac{\mathrm{d}^2 \hat{\Psi}'^0_{bt}}{\mathrm{d}r^2} + \frac{1}{r}\frac{\mathrm{d}\hat{\Psi}'^0_{bt}}{\mathrm{d}r} = \hat{Q}'^0_{bt}\ . \tag{48}$$

Since $\lambda_{\mathrm{bt}} = 0$ and $n = 0$ for this case, one of the terms in the radial structure equation has vanished, making the left side an exact differential. Equation (48) can therefore be integrated analytically between $r = a$ and $r = b$ to give

$$b\left.\frac{\mathrm{d}\hat{\Psi}'^0_{bt}}{\mathrm{d}r}\right|_{r=b} - a\left.\frac{\mathrm{d}\hat{\Psi}'^0_{bt}}{\mathrm{d}r}\right|_{r=a} = \int_a^b \hat{Q}'^0_{bt}\, r\,\mathrm{d}r\ . \tag{49}$$

We choose initial conditions for which the right side of this equation is zero, i.e. the barotropic PPV averaged over the 2-D annular domain is zero, and it is then guaranteed to remain so for all time, as shown in Section 2.3.1. This means that we need only explicitly set

$$\left.\frac{\mathrm{d}\hat{\Psi}'^{0}_{bt}}{\mathrm{d}r}\right|_{r=a} = 0 \tag{50}$$

and we will automatically have

$$\left.\frac{\mathrm{d}\hat{\Psi}'^{0}_{bt}}{\mathrm{d}r}\right|_{r=b} = 0 \tag{51}$$

from equation (49). If we explicitly set both (50) and (51) when solving (48) in this case, we therefore have an underconstrained problem. We need an additional constraint to close the solution.

We have defined two streamfunctions in the model — one per layer or, equivalently, one per vertical normal mode — and each of these has an integration constant associated with it (Section 2.1). Just because these two arbitrary constants have no physical meaning does not mean that they do not need to be defined in the numerical model. Now that we know that equations (50) and (51) are not independent boundary conditions, and therefore that to explicitly impose both would lead to an underconstrained PPV inversion, we choose to explicitly impose only equation (50). We then take the opportunity to use the remaining degree of freedom associated with the solution of equation (48) to define one of the streamfunction integration constants, by arbitrarily setting

$$\hat{\Psi}'^{0}_{bt}|_{r=b} = 0 \ , \tag{52}$$

which completes the set of two boundary conditions for the $m = \mathrm{bt}$, $n = 0$ case, and gives a well-posed problem.

Incidentally, the second streamfunction integration constant is defined by requiring the mean interface perturbation to be zero using equation (13), which follows from volume conservation for either layer. This requirement is imposed "off-line" by adding a suitably-chosen constant to one of the streamfunction fields when model diagnostics are plotted, and not as a boundary condition during the inversion.

A summary of the boundary conditions which we must explicitly set when integrating

	$n = 0$	$n \neq 0$
$m = \mathrm{bt}$	$\left.\frac{\mathrm{d}\hat{\Psi}'^{n}_{m}}{\mathrm{d}r}\right\|_{r=a} = 0$ $\hat{\Psi}'^{n}_{m}\|_{r=b} = 0$	$\hat{\Psi}'^{n}_{m}\|_{r=a} = 0$ $\hat{\Psi}'^{n}_{m}\|_{r=b} = 0$
$m = \mathrm{bc}$	$\left.\frac{\mathrm{d}\hat{\Psi}'^{n}_{m}}{\mathrm{d}r}\right\|_{r=a} = 0$ $\left.\frac{\mathrm{d}\hat{\Psi}'^{n}_{m}}{\mathrm{d}r}\right\|_{r=b} = 0$	$\hat{\Psi}'^{n}_{m}\|_{r=a} = 0$ $\hat{\Psi}'^{n}_{m}\|_{r=b} = 0$

Table 1: Summary of boundary conditions applied to the streamfunction when integrating the continuous equations. Because the diagnostic Helmholtz equation relating ψ and q is second order, two conditions (one at each boundary) are required for each combination of vertical and azimuthal normal modes, denoted by m and n respectively.

equation (41) is given in Table 1. With these conditions, the sidewall boundaries are impermeable to each component of the full flow — the solid-body rotation equilibrium flow, the mean flow correction and the eddy components. The boundaries are slippery to the solid-body rotation flow and the eddies, but no-slip to the mean flow correction.

In Section 3, we discretize the model equations so that they are in a form suitable for numerical integration.

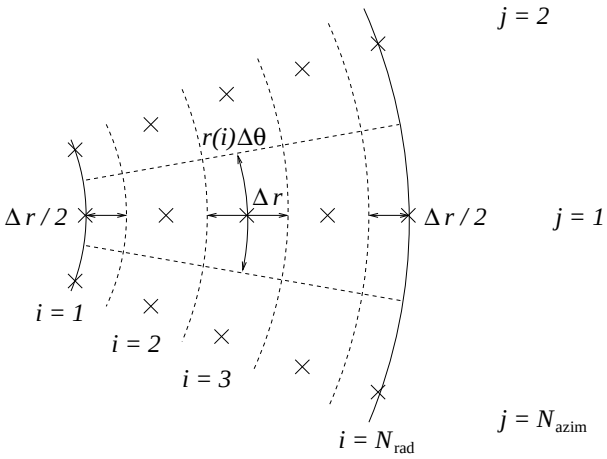

Figure 3: Definition of the model grid. Grid-points are marked with a "×" sign, grid-boxes with dashed lines, and the two cylindrical boundaries $r = a$ and $r = b$ with solid lines. The dimensions of typical grid-boxes, both in the interior and at the boundaries, are shown.

3 Discretization of the equations

3.1 The model grid

We have derived a set of model partial differential equations and boundary conditions which are both sensible and well-posed. We now discretize the equations so that they are suitable for numerical solution on a computer. We must take great care to ensure that the discretized equations and boundary conditions retain the important properties possessed by the continuous equations. In particular, it is important that they satisfy discretized analogues of the integral properties discussed in Section 2.3.

The regular grid on which we discretize the equations is shown in Figure 3. The grid consists of $N_{\rm rad}$ points in the radial dimension (including one point on each boundary $r = a$ and $r = b$), and $N_{\rm azim}$ points in the azimuthal dimension. We define

$$\Delta r = \frac{b-a}{N_{\rm rad}-1} \tag{53}$$

and

$$\Delta\theta = \frac{2\pi}{N_{\rm azim}} \ , \tag{54}$$

and then we have

$$r(i) = a + (i-1)\Delta r \ , \qquad i = 1, 2, \ldots, N_{\rm rad} \tag{55}$$

and

$$\theta(j) = j\Delta\theta \ , \qquad j = 1, 2, \ldots, N_{\rm azim} \ . \tag{56}$$

The point $(i, N_{\rm azim}+1)$ is the same as the point $(i, 1)$. We define the perturbation streamfunction $\psi'(i,j,k)$ and PPV $q'(i,j,k)$ at each of these points in each layer ($k = 1, 2$), so that ψ' and q' are co-located on the grid. The area of the gridbox with coordinates (i,j) is approximately $[1 - \frac{1}{2}\delta_{i,\,1} - \frac{1}{2}\delta_{i,\,N_{\rm rad}}]r(i)\Delta r\Delta\theta$, where $\delta_{*,*}$ is the Kronecker delta function.

3.2 Prognostic equations

In the continuous case, we chose perturbation streamfunction boundary conditions such that each of the three contributions (advection, forcing, dissipation) to the area-integrated perturbation PPV tendency was zero. We would now like to choose discretizations of these contributions, together with discretizations of the boundary conditions, for which this statement still holds *exactly*. If our discretization only conserves mean PPV approximately, then there is the possibility of a non-physical and explosive increase in the PPV, even if the error is small, due to the compound effects of very many timesteps. Following Section 2.3.1, we therefore next examine the discretizations and boundary conditions necessary to ensure that

$$\sum_{i=1}^{N_{\rm rad}} \sum_{j=1}^{N_{\rm azim}} [1 - \frac{1}{2}\delta_{i,1} - \frac{1}{2}\delta_{i,N_{\rm rad}}]\, f(i,j,k) r(i)\Delta r\Delta\theta = 0 \tag{57}$$

for $k = 1, 2$, where $f(i,j,k)$ is, in turn, the discretized azimuthal derivative, Jacobian and Laplacian.

3.2.1 Azimuthal derivative

The centred, second order discretization of the azimuthal derivative:

$$f(i,j,k) = \frac{\psi'(i,j+1,k) - \psi'(i,j-1,k)}{2\Delta\theta} \tag{58}$$

satisfies equation (57) unconditionally, as in the continuous case.

3.2.2 Jacobian

The second order Arakawa (1966) discretization of the Jacobian satisfies equation (57) if

$$\frac{\psi'(i,j+1,k)-\psi'(i,j,k)}{\Delta\theta}=0 \quad \forall\, j,k,i=1,N_{\rm rad}\ , \tag{59}$$

which is a discretized version of the condition (46) for the continuous case.

3.2.3 Laplacian

It is tedious but straightforward to show that the five-point discretization of the Laplacian (whose continuous definition is given in equation (17) for reference):

$$\begin{aligned} f\ &(i,j,k) \\ =\ &\frac{\psi'(i+1,j,k)-2\psi'(i,j,k)+\psi'(i-1,j,k)}{(\Delta r)^2} \\ +\ &\frac{\psi'(i+1,j,k)-\psi'(i-1,j,k)}{2r(i)\Delta r} \\ +\ &\frac{\psi'(i,j+1,k)-2\psi'(i,j,k)+\psi'(i,j-1,k)}{[r(i)\Delta\theta]^2} \end{aligned} \tag{60}$$

with *ghost point* values $\psi'(0,j,k)$ and $\psi'(N_{\rm rad}+1,j,k)$ given by linear extrapolation:

$$\begin{aligned} \psi'(2,j,k)-\psi'(1,j,k) \quad &= \\ \psi'(1,j,k)-\psi'(0,j,k) \quad &\end{aligned} \tag{61}$$

and

$$\begin{aligned} \psi'(N_{\rm rad}+1,j,k)-\psi'(N_{\rm rad},j,k) \quad &= \\ \psi'(N_{\rm rad},j,k)-\psi'(N_{\rm rad}-1,j,k) \quad &, \end{aligned} \tag{62}$$

satisfies equation (57) if

$$\sum_{j=1}^{N_{\rm azim}} \frac{\psi'(2,j,k)-\psi'(1,j,k)}{\Delta r}=0 \quad \forall\, k \tag{63}$$

and

$$\sum_{j=1}^{N_{\rm azim}} \frac{\psi'(N_{\rm rad},j,k)-\psi'(N_{\rm rad}-1,j,k)}{\Delta r}=0 \quad \forall\, k\ , \tag{64}$$

which are discretized versions of the condition (47) for the continuous case. There will be a small error in the value of the calculated discretized Laplacian at the boundaries due to the assumption of linearly-extrapolated ghost points, but there is no other simple way to discretize the Laplacian in such a way that analogues of its integral properties are fully preserved.

3.3 Diagnostic equations

The discretized versions of equations (39) and (40) are

$$\Psi'_m(i,j)=\sum_{n=0}^{N_{\rm azim}-1}\hat{\Psi}'^n_m(i)e^{2\pi\sqrt{-1}nj/N_{\rm azim}} \tag{65}$$

and

$$Q'_m(i,j)=\sum_{n=0}^{N_{\rm azim}-1}\hat{Q}'^n_m(i)e^{2\pi\sqrt{-1}nj/N_{\rm azim}}\ . \tag{66}$$

The summations have been truncated, compared to equations (39) and (40), because there are only $N_{\rm azim}$ independent Fourier components associated with the discrete Fourier transform of a series of $N_{\rm azim}$ numbers.

Because $\Psi'_m(i,j)$ is real, we have

$$\hat{\Psi}'^{N_{\rm azim}-n}_m(i)=\left[\hat{\Psi}'^n_m(i)\right]^* \tag{67}$$

for $n=1,2,\ldots,N_{\rm azim}-1$. We choose $N_{\rm azim}$ to be even, and then we need only explicitly solve equation (41) for $n=0,1,2,\ldots,N_{\rm azim}/2$. Solutions for $n=N_{\rm azim}/2+1,\ldots,N_{\rm azim}-1$ are given in terms of solutions for $n=N_{\rm azim}/2-1,\ldots,1$ by equation (67), halving the processing time required for the PPV inversions. The maximum resolvable wavenumber is the Nyquist wavenumber, $N_{\rm azim}/2$.

In terms of the normal mode variables, the discretized boundary conditions (59), (63) and (64) reduce, on substitution into equations (65) and (66), to

$$\left.\begin{aligned} \hat{\Psi}'^n_m(1) &= 0 \\ \hat{\Psi}'^n_m(N_{\rm rad}) &= 0 \end{aligned}\right\} \quad \forall\, m,n\neq 0 \tag{68}$$

and

$$\left.\begin{aligned} \hat{\Psi}'^0_m(1) &= \hat{\Psi}'^0_m(2) \\ \hat{\Psi}'^0_m(N_{\rm rad}) &= \hat{\Psi}'^0_m(N_{\rm rad}-1) \end{aligned}\right\} \quad \forall\, m\ . \tag{69}$$

We now consider the discretization of the radial structure equation (41). Using centred three-point finite differences at the interior points $i=2,3,\ldots,N_{\rm rad}-1$, we obtain

$$\begin{aligned} &\frac{\hat{\Psi}'^n_m(i-1)-2\hat{\Psi}'^n_m(i)+\hat{\Psi}'^n_m(i+1)}{(\Delta r)^2} \\ &\quad+\frac{\hat{\Psi}'^n_m(i+1)-\hat{\Psi}'^n_m(i-1)}{2r(i)\Delta r} \\ &\quad-\left[\lambda_m+\frac{n^2}{[r(i)]^2}\right]\hat{\Psi}'^n_m(i)=\hat{Q}'^n_m(i)\ . \end{aligned} \tag{70}$$

Re-grouping terms according to grid-points gives

$$\alpha^-(i)\hat{\Psi}'^n_m(i-1)+\gamma(i)\hat{\Psi}'^n_m(i)+\alpha^+(i)\hat{\Psi}'^n_m(i+1) = \hat{Q}'^n_m(i)(\Delta r)^2 \ , \qquad (71)$$

where the dimensionless quantities $\alpha^\pm$ and γ are given by

$$\alpha^\pm(i) = 1 \pm \frac{\Delta r}{2r(i)} \qquad (72)$$

and

$$\gamma(i) = -2 - \left[\lambda_m + \frac{n^2}{[r(i)]^2}\right](\Delta r)^2 \ . \qquad (73)$$

In Cartesian geometry we would have $\alpha^\pm(i) = 1$.

The $N_{\rm rad} - 2$ equations (71), together with 2 boundary conditions, complete the set of $N_{\rm rad}$ equations in the $N_{\rm rad}$ unknowns $\hat{\Psi}'^n_m(i)$, $i = 1, 2, \ldots, N_{\rm rad}$. These linear equations can be written in matrix form:

$$\begin{pmatrix} \text{bdy} & \text{bdy} & & & & \ldots \\ \alpha^-(2) & \gamma(2) & \alpha^+(2) & & & \ldots \\ & \alpha^-(3) & \gamma(3) & \alpha^+(3) & & \ldots \\ & & \alpha^-(4) & \gamma(4) & \alpha^+(4) & \ldots \\ & & & \alpha^-(5) & \gamma(5) & \ldots \\ \vdots & \vdots & \vdots & \vdots & \vdots & \ddots \end{pmatrix} \times \begin{pmatrix} \hat{\Psi}'^n_m(1) \\ \hat{\Psi}'^n_m(2) \\ \hat{\Psi}'^n_m(3) \\ \hat{\Psi}'^n_m(4) \\ \hat{\Psi}'^n_m(5) \\ \vdots \end{pmatrix} = \begin{pmatrix} 0 \\ \hat{Q}'^n_m(2)(\Delta r)^2 \\ \hat{Q}'^n_m(3)(\Delta r)^2 \\ \hat{Q}'^n_m(4)(\Delta r)^2 \\ \hat{Q}'^n_m(5)(\Delta r)^2 \\ \vdots \end{pmatrix} \qquad (74)$$

where the zero elements in the tridiagonal $N_{\rm rad}$ by $N_{\rm rad}$ matrix have been left blank. The two elements labelled "bdy" are boundary condition elements, dependent upon m and n, and there are two more such elements in the final two columns of the bottom row.

3.4 Perturbation streamfunction boundary conditions for the discretized equations

In the continuous case, we found that the boundary conditions for the barotropic mean flow correction component (m = bt, $n = 0$) were ill-posed as originally stated, and remained so until we replaced a redundant boundary condition with an equation to define an integration constant. This happens in the discretized case, too: the square matrix in equation (74) is singular for the barotropic mean flow correction, when the boundary condition elements "bdy" are $(-1, 1)$ in the top row and $(1, -1)$ in the bottom row. The analytical proof of this, which involves showing that a certain linear combination of rows is zero, is tedious but straightforward. By analogy with the continuous case, we replace the two boundary condition elements in the bottom row with $(0, 1)$ to define the integration constant by setting the streamfunction for this component to zero on the outer boundary, and then the matrix is no longer singular (typical condition numbers are given in Section 4.5).

In the continuous system, we set the $n = 0$, m = bt normal streamfunction derivative to zero at one boundary and found that, if the mean barotropic PPV was zero, the streamfunction derivative would automatically be zero at the other boundary. Importantly, in contrast with the continuous system, this statement does not hold exactly for the discretized system. This is because $\hat{Q}'^n_m(1)$ and $\hat{Q}'^n_m(N_{\rm rad})$ do not appear in equation (74); we do not apply the discretized differential equation at the boundaries, as we need to use these two degrees of freedom to set the boundary conditions.

The error corresponding to this PPV leak is small ($\sim (\Delta r)^2$), but even small errors can grow to dominate the solution after a large number of timesteps. To fix this problem with the barotropic mean flow correction, we discard the outer boundary streamfunction $\hat{\Psi}'^0_{\rm bt}(N_{\rm rad})$ obtained through inversion of equation (74) and define a new value for it by setting $\hat{\Psi}'^0_{\rm bt}(N_{\rm rad}) = \hat{\Psi}'^0_{\rm bt}(N_{\rm rad} - 1)$. This ensures that the boundary conditions (69) required for conservation of mean PPV are satisfied exactly, but the consequence is that the discretized differential equation (70) is not exactly satisfied at the point $N_{\rm rad} - 1$. The imposed boundary conditions are summarized in Table 2.

3.5 Details of the numerical schemes

3.5.1 Time stepping

For the time stepping we use a leapfrog scheme with a Robert (1966) three-level time filter applied at each timestep, to suppress the computational mode splitting between even and odd numbered

	$n = 0$	$n \neq 0$
$m = \mathrm{bt}$	$\hat{\Psi}'^{n}_{m}(2) - \hat{\Psi}'^{n}_{m}(1) = 0$ $\hat{\Psi}'^{n}_{m}(N_{\mathrm{rad}}) = 0^{\dagger}$	$\hat{\Psi}'^{n}_{m}(1) = 0$ $\hat{\Psi}'^{n}_{m}(N_{\mathrm{rad}}) = 0$
$m = \mathrm{bc}$	$\hat{\Psi}'^{n}_{m}(2) - \hat{\Psi}'^{n}_{m}(1) = 0$ $\hat{\Psi}'^{n}_{m}(N_{\mathrm{rad}}) - \hat{\Psi}'^{n}_{m}(N_{\mathrm{rad}} - 1) = 0$	$\hat{\Psi}'^{n}_{m}(1) = 0$ $\hat{\Psi}'^{n}_{m}(N_{\mathrm{rad}}) = 0$

Table 2: Summary of the boundary conditions applied to the streamfunction when integrating the discretized equations. The analogous conditions for the for the continuous case are given in Table 1. †After the inversion, $\hat{\Psi}'^{0}_{\mathrm{bt}}(N_{\mathrm{rad}})$ is redefined by $\hat{\Psi}'^{0}_{\mathrm{bt}}(N_{\mathrm{rad}}) - \hat{\Psi}'^{0}_{\mathrm{bt}}(N_{\mathrm{rad}} - 1) = 0$, as discussed in the text.

steps (Mesinger & Arakawa, 1976). At each step, of size Δt, q^{t+1} is determined at each grid point using the leapfrog scheme:

$$q^{t+1} = q^{t-1} + 2\Delta t \;\; q^{t}_{\mathrm{tendency}} \;, \qquad (75)$$

and then the value of q^t is adjusted in such a way as to move it closer to the mean of q^{t-1} and q^{t+1}:

$$q^{t} \rightarrow q^{t} + R\left(\frac{q^{t-1} + q^{t+1}}{2} - q^{t}\right) \;. \qquad (76)$$

The old value of q^t is abandoned and the new, filtered value is used in its place. The *Robert filter parameter* $R > 0$ is chosen to be as small as possible whilst still suppressing the leapfrog decoupling.

3.5.2 Time-lagged diffusion

Numerical solutions of the simple diffusion equation, using the leapfrog scheme for the time-discretization and a time-centred three-point finite difference for the space-discretization, are unconditionally unstable due to a computational mode (Haltiner & Williams, 1980). To avoid this in the present model, we time-lag the diffusion terms by one timestep when evaluating the right sides of the discretized analogues of equations (23) and (24). This means that, when evaluating the PPV tendency at timestep t, we calculate the forcing ($\partial/\partial\theta$) and advection ($J(\psi'_i, q'_i)$) terms using the fields at timestep t, but calculate the diffusion (∇^2) terms using the fields at timestep $t-1$.

3.5.3 Hyperdiffusion

To represent sub-gridscale effects we add a hyperdiffusion term to the right sides of the prognostic equations (23) and (24), as is usual in numerical models (e.g. Lewis, 1992).

At first, a fourth-order streamfunction hyperdiffusion term $\nu_{\mathrm{hyper}}\nabla^4\psi'_i$ was tried, but significant gridscale features were always found to form at the lateral boundaries whenever the model was run. This is because during the PPV inversion, any gridscale features in the PPV field will give rise to corresponding grid-scale features in the perturbation streamfunction field, and then the $\nu_{\mathrm{hyper}}\nabla^4\psi'$ contribution to the PPV tendency will tend to damp out these features in the PPV field. Unfortunately this does not happen at the boundaries in the discretized system, because boundary values of the PPV are not used when performing the inversion. As already discussed, $\hat{Q}'^{n}_{m}(1)$ and $\hat{Q}'^{n}_{m}(N_{\mathrm{rad}})$ are missing from equation (74). Values of PPV therefore are able to feed back into the PPV tendency field only at interior points, and there is nothing to suppress grid-scale features in the PPV field at the boundaries.

To avoid this, we instead use second-order hyperdiffusion applied to the PPV, by adding a term $\nu_{\mathrm{hyper}}\nabla^2 q'_i$ to the prognostic equations. This term is also time-lagged by one timestep, as discussed above. The hyperdiffusion term does not exactly satisfy equation (57), though the error is small. In order to keep the model solutions as close as possible to the continuous equations solutions, we periodically reset the mean PPV to zero in the model, by adding a very small constant whose value is chosen to satisfy this requirement.

3.5.4 Stochastic parameterization of sub-gridscale effects

As a way of representing sub-gridscale effects, additional and complementary to the hyperdiffusion representation discussed above, there is the

option of a stochastic representation in QUAGMIRE. Such parameterizations are becoming more popular in numerical models, with the recognition that the additional model degrees of freedom introduced by a stochastic parameterization may be able to compensate, at least partially, for the degrees of freedom associated with sub-gridscale motions missing from the model (Williams et al., 2003).

We choose the simplest possible form for the stochastic noise terms. At each gridpoint and at each timestep, a random number is drawn from the uniform distribution on the interval $[0, 1]$, and then shifted to the interval $[-\text{amp}, \text{amp}]$ before being used as an additive contribution to the PPV tendency. The constant *amp* is a given amplitude with units s^{-2}. The discretized noise fields so defined contain no correlations in either time or horizontal position.

3.6 Summary of numerical integration scheme

Flow charts summarizing the details of the QUAGMIRE numerical integration scheme are shown in Figures 4 and 5. Given the PPV fields at times $t-1$ and t, we invert to obtain the streamfunction fields at those times, which then allows us to calculate all the contributions to the PPV tendency. We perform a leapfrog time integration to obtain the PPV field at time $t+1$, and then modify the PPV field at time t by applying a Robert filter. Once we have obtained $q'(t)$ and $q'(t+1)$ from $q'(t-1)$ and $q'(t)$, we discard $q'(t-1)$ and $\psi'(t-1)$, we dump $q'(t)$ and $\psi'(t)$ to disk if required, then we re-label $t \to t-1$ and begin the loop again. Note that the streamfunction and PPV must be kept in memory at three consecutive timesteps.

The system state is completely determined by ψ'. Note that it is also completely determined by q' together with the boundary conditions, because equations (25) and (26) are uniquely invertible. It is not necessary to dump both ψ' and q' to disk in order to have a complete description of the system, therefore. Nevertheless, we choose to save both fields, in order to reduce the need for further calculations when plotting model diagnostics.

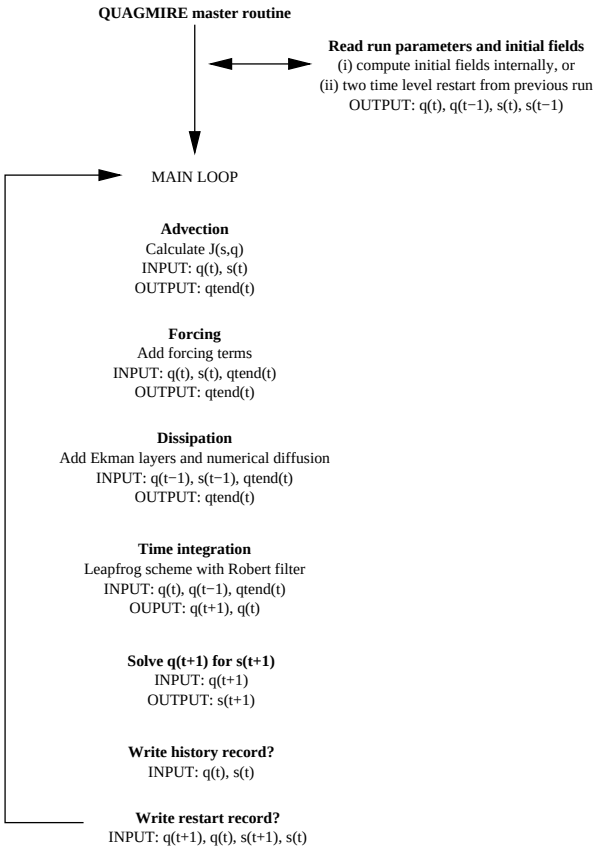

Figure 4: Organigram giving an overview of how the model integrations progress. The perturbation potential vorticity is labelled q, and the perturbation streamfunction is labelled s.

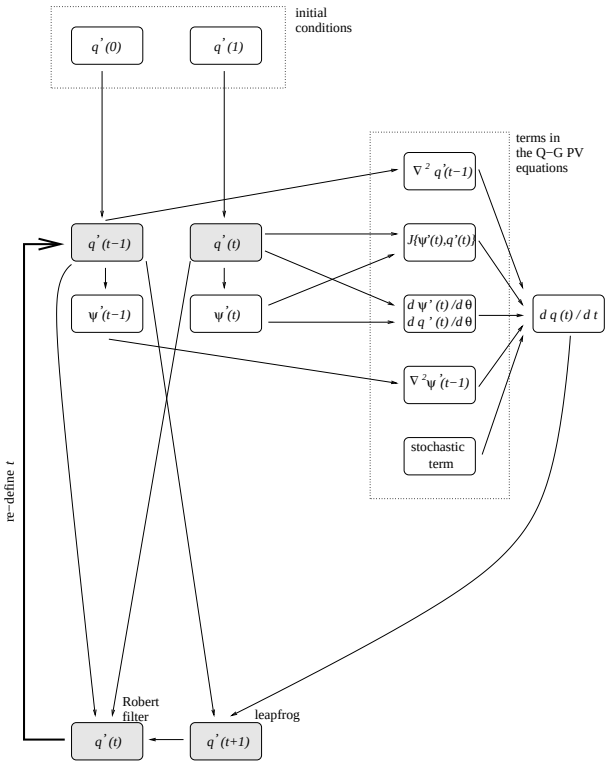

Figure 5: Organigram showing in detail how the the model integrations progress, starting with initial conditions $q'(0)$ and $q'(1)$. Each timestep has inputs $q'(t-1)$ and $q'(t)$ and outputs $q'(t)$ and $q'(t+1)$, shown shaded. $J(\psi', q') = [(\partial\psi'/\partial r)(\partial q'/\partial\theta) - (\partial\psi'/\partial\theta)(\partial q'/\partial r)]/r$ is the Jacobian.

3.7 Initial conditions

A feature of the leapfrog timestepping scheme is that initial condition fields are required at two separate times, in order to begin the integration. As shown in Figure 5, we choose to specify the PPV fields as initial conditions. We use small amplitude random noise for these fields, seeding the system to permit the growth of unstable perturbations of any azimuthal and radial wavenumber. The intrinsic Fortran function `RANDOM_NUMBER` is used to generate random numbers with a uniform distribution which are shifted to a chosen symmetrical interval centred on zero. We then subtract the mean PPV in each layer at both timesteps, which makes the fields satisfy the zero mean barotropic PPV condition of Sections 2.3.2 and 3.4.

4 Technical model details

4.1 Model source code

Code to carry out the numerical integrations described herein has been written in Fortran 95, and compiled using the Numerical Algorithms Group (NAG) f95 compiler for Linux. Routines from the NAG library are employed: `nag_fft` for the transformations between physical and spectral space described by equations (65) and (66), `nag_gen_bnd_lin_sys` for solving the complex band matrix equation (74) a large number $(N_{\rm azim} + 2)$ of times each timestep, and `nag_math_constants` for the value of π.

The model source code consists of 15 `.f90` subroutines in the `src/` directory. In total, there are 1200 lines of code in these subroutines, many of which are comments. Brief descriptions of the subroutines are now given.

- `modules.f90` declares the global variables, categorized into five modules: `precision` (the numerical precisions for the calculations and dumps to disk), `dyn_vars` (the dynamical state arrays, i.e. streamfunction and PPV, which are updated once per timestep), `solver_vars` (the permanent solver arrays, calculated once at the start of the model run), `phys_params` (the physical parameters, including system dimensions and rotation rates) and `grid_params` (the numerical parameters, including grid spacings and timesteps).

- `main.f90` is the highest-level routine in the model, making one-off calls to `init_model.f90`, `init_solver.f90` and `init_state.f90`, and then calling in turn, from within the time stepping loop, `jacobian.f90`, `forcing.f90`, `dissipation.f90`, `step_q.f90`, `solver.f90` and `save_fields.f90`.

- `init_model.f90` initializes the model by reading the namelist (Section 4.3), and then allocating and evaluating the parameters declared in the `phys_params` and `grid_params` modules.

- `init_solver.f90` initializes the solver by allocating and evaluating the arrays declared in the `solver_vars` module.

- `init_state.f90` initializes the model state by allocating and evaluating starting values for the arrays declared in the `dyn_vars` module. This subroutine makes calls to `read_pu_fields.f90` and `read_forcing_fields.f90`.

- `jacobian.f90` calculates the advection $(J(\psi_i', q_i'))$ term in cylindrical polar coordinates, storing the result as a PPV tendency. The formula is written to minimise the number of multiplications, which are computationally more expensive than additions.

- `forcing.f90` calculates the forcing $(\partial/\partial\theta)$ terms (forcing of perturbations by the mean flow, topographic forcing, stochastic forcing and optional relaxation to a specified PPV field), adding the result to the PPV tendency. This subroutine makes calls to `dtheta.f90`.

- `dissipation.f90` calculates the dissipation (∇^2) terms (Ekman layers at the upper and lower boundaries, Ekman layers at the internal interface and 2nd order PPV hyperdiffusion), adding the result to the PPV tendency. This subroutine makes calls to `laplacian.f90`.

- `step_q.f90` uses the PPV tendency to perform the timestepping, with a Robert three-level time filter, and thereby updates the PPV field.

- `solver.f90` solves the Helmholtz equation in cylindrical polar co-ordinates, to update the streamfunction field given the updated PPV field

- `save_fields.f90` dumps the model state (streamfunction and PPV) to disk. The current state (regular dump) and/or the current and previous states (pickup dump) are saved as unformatted binary data.

- `read_pu_fields.f90` reads the initial model state from a pickup file, if required.

- `read_forcing_fields.f90` reads the forcing fields (`PSI_relax.bin` and `QGPV_relax.bin`) from disk, if required.

- `dtheta.f90` is the azimuthal derivative operator for calculating the forcing terms in the PPV equations.

- `laplacian.f90` is the Laplacian operator in cylindrical polar co-ordinates for calculating the dissipation terms in the PPV equations.

A `Makefile` is also included in the `src/` directory, to build the executable from the source code files. By typing `make` at a command prompt, each `.f90` source file is compiled to produce a corresponding `.o` object file, and then the 15 object files (plus object files from the NAG library) are linked to build the executable, with filename `qgam` and size around 400 kB.

4.2 Tests of the model code

The azimuthal derivative (`dtheta.f90`), Laplacian (`laplacian.f90`) and advection (`jacobian.f90`) routines were each tested using input fields consisting of random numbers satisfying the boundary conditions. The mean PPV tendency due to each contribution was found to be zero to within numerical precision, implying that the code for these routines is free from errors.

The Helmholtz solver routines (`init_solver.f90` and `solver.f90`) were tested by first using the forward formulae (25) and (26) with our discretized Laplacian (60)–(62) to calculate the PPV fields corresponding to given random perturbation streamfunction fields, and then using the routines to reconstruct the streamfunction fields from the calculated PPVs. The root-mean-square difference between the original and reconstructed streamfunction fields was around 0.1%, implying that the solver code was also free from errors. The reason that the agreement is not exact, to within numerical precision, is that we assume linearly-extrapolated ghost points to evaluate the Laplacian in the forward formulae — an assumption which is not made during the inversion.

4.3 Namelist

The namelist, `qgam.data`, should be copied to the working directory (i.e. the directory in which the model output is to appear), and then edited to alter the system/numerical details for the run. The entries in the namelist, which fall into five categories, are as follows.

GRID DEFINITION

- `N_rad` (INTEGER) = $N_{\rm rad}$ = number of grid points in the radial direction, including one point on each of the boundaries $r = a$ and $r = b$
- `N_azim` (INTEGER) = $N_{\rm azim}$ = number of grid points in the azimuthal direction
- `N_layer` (INTEGER) = number of layers (must be 100 at most; in the present model release, must be 2)

TIME STEPPING

- `delta_t` (REAL) = Δt = time step (s)
- `start_step` (INTEGER) = first step in the integration — set to 1 to internally compute the initial condition using random numbers, otherwise picks up from a previous calculation using the file labelled `start_step`
- `end_step` (INTEGER) = last step in the integration
- `Robert_filter_parameter` (REAL) = R = strength of Robert time-filtering — must be between 0.0 (no filtering) and 1.0 (full filtering)
- `dump_period` (INTEGER) = number of steps between successive regular dumps to disk
- `pickup_dump_period` (INTEGER) = number of steps between successive pickup dumps to disk
- `debug` (INTEGER) = debug messages switched on? (set to 1 for 'yes')

SYSTEM DIMENSIONS

- `a` (REAL) = a = radius of inner boundary (m)
- `b` (REAL) = b = radius of outer boundary (m)
- `H` (REAL) = H = depth of each layer (m)
- `s_top` (REAL) = $s_{\rm top}$ = radial slope of lid (dimensionless)
- `s_bot` (REAL) = $s_{\rm bot}$ = radial slope of base (dimensionless)

FLUID PROPERTIES

- `rho` (REAL) = ρ = density of each layer (kg m^{-3}) from top to bottom, i.e. vector of length `N_layer` with elements of increasing size
- `S` (REAL) = S = interfacial tension between each pair of adjacent layers (N m^{-1}) from top to bottom, i.e. vector of length `N_layer`-1

- `new` (REAL) = ν = kinematic viscosity of each layer ($m^2\ s^{-1}$) from top to bottom, i.e. vector of length `N_layer`

FORCING AND DISSIPATION

- `initial_amplitude` (REAL) = amplitude of initial PPV perturbation (s^{-1}) — only used if `start_step` is set to 1
- `omega` (REAL) = Ω = angular velocity of base (rad s^{-1}) — must be positive
- `lid_delta_omega` (REAL) = $\Delta\Omega$ = differential angular velocity of lid relative to base (rad s^{-1}) — can be either positive (prograde) or negative (retrograde)
- `g` (REAL) = g = acceleration due to gravity ($m\ s^{-2}$)
- `new_hyper` (REAL) = $\nu_{\rm hyper}$ = 2nd order PPV hyperdiffusion coefficient ($m^2\ s^{-1}$)
- `relax_rate` (REAL) = inverse time-scale for relaxation to specified PPV field (s^{-1}) — only used if `relax_type` is set to 2 or 3
- `relax_type` (INTEGER) = set to 1 to relax to a specified streamfunction field (`PSI_relax.bin`), set to 2 to relax to a specified PPV field (`QGPV_relax.bin`), or set to 3 to do both 1 and 2
- `reset_period` (INTEGER) = number of steps between successive resetting of the mean PPV to zero — set to 1 to reset at each step
- `internal_ekman` (INTEGER) = internal Ekman layers switched on? (set to 1 for 'yes')
- `noise_amp` (REAL) = (starting value of) stochastic forcing amplitude (s^{-2})
- `d_dt_noise_amp` (REAL) = rate of change of stochastic forcing amplitude (s^{-3})

4.4 Shell script

A shell script, `run_qgam`, is included with the model. To launch the model, type `run_qgam` at the command line from a directory containing a namelist file. This deletes any data files already present, copies the current version of the executable to the local directory, creates a temporary uncommented namelist file, creates a file of parameter values in a form suitable to be read by the Matlab diagnostic script, runs the model (piping system messages to the output file, `qgam.out`), and finally deletes the local version of the executable and the temporary namelist.

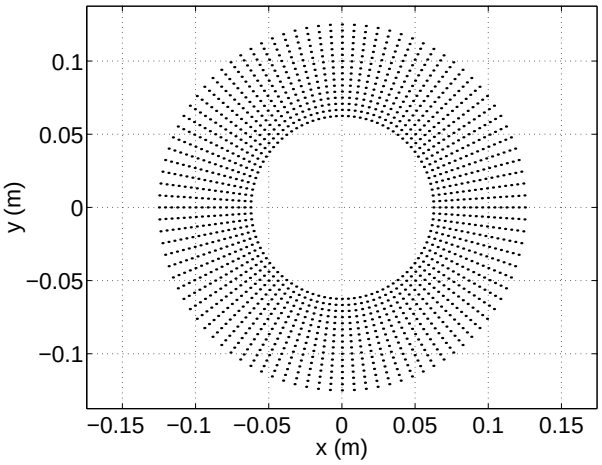

Figure 6: Typical gridpoint positions. In this case, there are 96 points in the azimuthal direction and 16 in the radial direction, giving gridboxes which are approximately square near the inner boundary. This figure was produced using option 11 of the Matlab diagnostics package (Section 4.6).

To avoid deleting pre-existing data files (e.g. for a pick-up run), use `run_qgam pu`.

4.5 Suitable values for the numerical parameters

The NAG FFT subroutines are much faster if the only prime factors of $N_{\rm azim}$ are 2, 3 and 5, and so a typical grid might be defined by $N_{\rm azim} = 2^5 \times 3 = 96$ and $N_{\rm rad} = 16$, as shown in Figure 6. A suitable Robert filter parameter is usually around $R = 0.01$. For given Ω and $\Delta\Omega$, we can take the amplitude of the random initial PPV perturbation to be $\Delta\Omega/100$ so that we are assessing the growth of very small perturbations, we can choose the timestep Δt to be such that the azimuthal Courant number $\frac{1}{2}\Delta\Omega\Delta t/\Delta\theta$ is 0.01, and we can choose the hyperdiffusion coefficient $\nu_{\rm hyper}$ to be such that the e-folding time $1/(\nu_{\rm hyper}\, k^2_{\rm Nyquist})$ for damping of mid-radius gridscale waves with the Nyquist wave vector

	m=bt	m=bc
$n = 0$	389	59
$n = 1$	112	35
$n = 2$	99	33
$n = 3$	82	31
$n = 4$	67	29
$n = 5$	54	26
$n = 6$	44	24
$n = 7$	36	21
$n = 8$	31	19
$n = 9$	26	17

Table 3: Estimates of the condition numbers (in the infinity-norm) of the tridiagonal matrices in equation (74), corresponding to the first 10 azimuthal modes for both of the vertical modes. Values given are rounded to the nearest integer, for typical run parameters.

$k_{\rm Nyquist} = N_{\rm azim}/(a+b)$ is equal to one lid rotation period, $2\pi/\Delta\Omega$.

It is recommended that model runs are performed using double numerical precision (retaining 16 significant figures) for the calculations and pick-up dumps to disk, and single numerical precision (retaining 8 significant figures) for the regular dumps. These are the default settings, hard-coded in `modules.f90`, and allow for accurate calculations as well as efficient data storage.

The factor by which relative errors in the perturbation streamfunction are greater than relative errors in the PPV, following solution of equation (74), is known as the *condition number* of the tridiagonal matrix in that equation. Some typical condition numbers for the matrices in equations (74) are shown in Table 3. The largest condition number in the system has a value of a few hundred, implying that only the last two significant figures of the inferred perturbation streamfunctions will be uncertain, and that errors due to rounding are therefore small.

In order to demonstrate insensitivity to the numerical parameters, comparative runs have been performed with (separately) the hyperdiffusion coefficient decreased by a factor of 10, the Robert filter parameter decreased by a factor of 10 and the gridspacing doubled in both directions, but all other parameters unmodified. The equilibrated wave number was the same in each case, and the mid-radius wave amplitude and phase speed differed by at most 0.3%. We have therefore demonstrated that both rounding errors and discretization errors are small, and that the equilibrated state is insensitive to the values of the numerical parameters, implying that the model output gives an accurate representation of the true solutions of the continuous model equations.

The code is very efficient: on a desktop Linux workstation with a 1.4 GHz *AMD Athlon* processor and 100% of the CPU usage, and with $N_{\rm azim} = 96$ and $N_{\rm rad} = 16$, a model integration speed of 120 timesteps per second is attained. In this case, it is found that timesteps of up to around 0.1 s can be used stably, implying that the model can run ten times faster than the laboratory annulus. The run-time memory requirement is 3.1 MB.

4.6 Matlab diagnostics

A Matlab diagnostics package (`diagnostic.m`, `diagnostic_read.m` and `gradient_imp.m`) is supplied with the model, consisting of 2100 lines of code. The package allows the model data and many other derived quantities to be plotted in cylindrical geometry with ease. To run the package, launch Matlab from the data directory and type `diagnostic.m`. The data file created by the shell script is read, and the following options are offered.

- 0 = exit
- 1 = contour plot of perturbation streamfunction
- 2 = contour plot of perturbation potential vorticity
- 3 = contour plot of perturbation interface height
- 4 = vector plot of perturbation velocity field
- 5 = contour plot of full streamfunction
- 6 = contour plot of full potential vorticity
- 7 = contour plot of full interface height
- 8 = vector plot of full velocity field

- 9 = time-series of mid-radius interface height wave amplitude
- 10 = multiple cartesian diagnostics
- 11 = plot of gridpoint positions
- 12 = time-series of mid-radius interface height
- 13 = option 1 over-plotted with option 4
- 14 = option 5 over-plotted with option 8
- 15 = time-series of radially-averaged zonal perturbation velocity
- 16 = mid-radius perturbation potential vorticity Hovmüller diagram
- 17 = mid-radius perturbation streamfunction Fourier spectrum
- 18 = contour plot of Lighthill Radiation Term magnitude
- 19 = contour plot of Brown's CAT indicator
- 20 = vector plot of full velocity shear field
- 21 = time-series of 1/4 and 3/4-radius interface height wave amplitude
- 22 = contour plot of local Richardson number in interfacial Ekman layer
- 23 = time series of minimum local Richardson number in interfacial Ekman layer
- 24 = contour plot of turbulent energy dissipation rate
- 25 = interface height profiles as a function of theta
- 26 = time series of system energy
- 27 = 3-D image of full interface height
- 28 = multiple radiation diagnostics
- 29 = contour plot of horizontal divergence
- 30 = mid-radius interface height Hovmüller diagram
- 31 = zonally-averaged zonal velocity as a function of radius
- 32 = time-radius Hovmüller plot of zonally-averaged zonal velocity

Simply select the option required, and follow the on-screen instructions to display the plot on the screen. To save or print a figure, first produce it using the appropriate option, then exit the diagnostics package using option 0 and issue the appropriate Matlab print command.

5 Closing remarks

5.1 Summary

The QUAGMIRE model described herein has been run extensively, and a detailed comparison between model and laboratory flows has been carried out Williams (2003). The model waves, which grow due to baroclinic instability if the Froude number is supercritical but otherwise decay, have phase speeds, equilibrated amplitudes and wavenumbers which agree well with those determined from the corresponding laboratory experiments. For Froude numbers which are higher still, more complicated model flows result, such as amplitude vacillations with reasonable amplitudes and periods and, ultimately, flow which is highly irregular and appears to be chaotic. The reasonable model/laboratory agreement provides an important validation of the model, and indicates that the numerical techniques employed are reliable.

5.2 Future plans

As with any numerical model, one can imagine many additions and improvements which could be made to the current version of QUAGMIRE. The most obvious and pressing of these is to generalize the model to apply to a general, user-specified number of superposed fluid layers, each of a (different) user-specified resting depth, rather than the current configuration of two layers of equal volume. In terms of more cosmetic aspects, it would be preferable if the data dumps to disk were in a portable, self-describing format, e.g. netCDF.

It is hoped that these and other changes will be implemented in the coming months and years, as QUAGMIRE continues to evolve.

References

Appleby, J. C. (1982). *Comparative theoretical and experimental studies of baroclinic waves in a two-layer system*. Ph.D. thesis, University of Leeds.

Arakawa, A. (1966). Computational design for long-term numerical integration of the equations of fluid motion: two-dimensional incompressible flow. *J. Comp. Phys.*, **1**, 119–143.

Boas, M. L. (1983). *Mathematical methods in the physical sciences*. Wiley, second edition.

Brugge, R., Nurser, A. J. G., & Marshall, J. C. (1987). A quasi-geostrophic ocean model: some introductory notes. Technical report, Blackett Laboratory, Imperial College, London.

Carrigan, C. R. (1978). Instability of a two-layer baroclinic flow in a channel. *Tellus*, **30**, 468–471.

Cattaneo, F. & Hart, J. E. (1990). Multiple states for quasi-geostrophic channel flows. *Geophys. Astrophys. Fluid Dyn.*, **54**, 1–33.

Charney, J. G. (1955). The use of the primitive equations of motion in numerical prediction. *Tellus*, **7**, 22–26.

Charney, J. G., Fjørtoft, R., & von Neumann, J. (1950). Numerical integration of the barotropic vorticity equation. *Tellus*, **2**(4), 237–254.

Daley, R. (1982). A non-iterative procedure for the time integration of the balance equations. *Monthly Weather Rev.*, **110**, 1821–1830.

Davey, M. K. (1978). Recycling flow over bottom topography in a rotating annulus. *J. Fluid Mech.*, **87**(3), 497–520.

Douglas, J. F. & Gasiorek, J. M. K. (2000). *Fluid Mechanics*. Pearson Higher Education.

Gill, A. E. (1982). *Atmosphere-Ocean Dynamics*. Academic Press.

Haltiner, G. J. & Williams, R. T. (1980). *Numerical prediction and dynamic meteorology*. Wiley, 2nd edition.

Hide, R. (1977). Experiments with rotating fluids. *Q. J. R. Meteorol. Soc.*, **103**(435), 1–28.

Hide, R., Mason, P. J., & Plumb, R. A. (1977). Thermal convection in a rotating fluid subject to a horizontal temperature gradient: spatial and temporal characteristics of fully developed baroclinic waves. *J. Atmos. Sci.*, **34**, 930–950.

Hignett, P., White, A. A., Carter, R. D., Jackson, W. D. N., & Small, R. M. (1985). A comparison of laboratory measurements and numerical simulations of baroclinic wave flows in a rotating cylindrical annulus. *Q. J. R. Meteorol. Soc.*, **111**, 131–154.

King, J. C. (1979). *Instabilities and nonlinear wave interactions in a two-layer rotating fluid*. Ph.D. thesis, University of Leeds.

Kwon, H. J. & Mak, M. (1988). On the equilibration in nonlinear barotropic instability. *J. Atmos. Sci.*, **45**(2), 294–308.

Lewis, S. R. (1992). A quasi-geostrophic numerical model of a rotating internally heated fluid. *Geophys. Astrophys. Fluid Dyn.*, **65**, 31–55.

Lovegrove, A. F. (1997). *Bifurcations and instabilities in rotating two-layer fluids*. Ph.D. thesis, Oxford University.

Lynch, P. (1989). The slow equations. *Q. J. R. Meteorol. Soc.*, **115**, 201–219.

McIntyre, M. E. (1967). *Convection and baroclinic instability in rotating fluids*. Ph.D. thesis, Cambridge University.

McIntyre, M. E. & Norton, W. A. (2000). Potential vorticity inversion on a hemisphere. *J. Atmos. Sci.*, **57**, 1214–1235.

McWilliams, J. C. & Gent, P. R. (1980). Intermediate models of planetary circulations in the atmosphere and ocean. *J. Atmos. Sci.*, **37**(8), 1657–1678.

Mesinger, F. & Arakawa, A. (1976). Numerical methods used in atmospheric models. *Global Atmospheric Research Programme Publications Series No. 17*.

Moura, A. D. (1976). The eigensolutions of the linearized balance equations over a sphere. *J. Atmos. Sci.*, **33**, 877–907.

Mundt, M. D., Brummell, N. H., & Hart, J. E. (1995). Linear and nonlinear baroclinic instability with rigid sidewalls. *J. Fluid Mech.*, **291**, 109–138.

Pedlosky, J. (1964). The stability of currents in the atmosphere and the ocean: Part I. *J. Atmos. Sci.*, **21**, 201–219.

Pedlosky, J. (1970). Finite-amplitude baroclinic waves. *J. Atmos. Sci.*, **27**, 15–30.

Pedlosky, J. (1971). Finite-amplitude baroclinic waves with small dissipation. *J. Atmos. Sci.*, **28**, 587–597.

Pedlosky, J. (1972). Limit cycles and unstable baroclinic waves. *J. Atmos. Sci.*, **29**, 53–63.

Pedlosky, J. (1987). *Geophysical Fluid Dynamics*. Springer-Verlag.

Phillips, N. A. (1954). Energy transformations and meridional circulations associated with simple baroclinic waves in a two-level, quasi-geostrophic model. *Tellus*, **3**, 273–286.

Phillips, N. A. (1956). The general circulation of the atmosphere: a numerical experiment. *Q. J. R. Meteorol. Soc.*, **82**(352), 123–164.

Phillips, N. A. (1963). Geostrophic motion. *Rev. Geophys.*, **1**(2), 123–176.

Read, P. L., Collins, M., Früh, W.-G., Lewis, S. L., & Lovegrove, A. F. (1998). Wave interactions and baroclinic chaos: a paradigm for long timescale variability in planetary atmospheres. *Chaos, Solitons and Fractals*, **9**(1/2), 231–249.

Reynolds, O. (1883). An experimental investigation of the circumstances which determine whether the motion of water shall be direct or sinuous, and of the law of resistance in parallel channels. *Phil. Trans. R. Soc. London*, **174**, 935–982.

Robert, A. J. (1966). The integration of a low order spectral form of the primitive meteorological equations. *J. Meteor. Soc. Japan*, **44**(5), 237–245.

Salmon, R. & Talley, L. D. (1989). Generalizations of Arakawa's Jacobian. *J. Comp. Phys.*, **83**, 247–259.

Smith, R. K. (1974). On limit cycles and vacillating baroclinic waves. *J. Atmos. Sci.*, **31**, 2008–2011.

Smith, R. K. (1977). On a theory of amplitude vacillation in baroclinic waves. *J. Fluid Mech.*, **79**(2), 289–306.

Smith, R. K. & Pedlosky, J. (1975). A note on a theory of vacillating baroclinic waves *and* Reply. *J. Atmos. Sci.*, **32**, 2027.

Stephen, A. V. (1998). *POD methods in baroclinic flows*. Ph.D. thesis, University of Oxford.

Vettin, F. (1884). Experimentelle Darstellung von Luftbewegungen unter dem Einfluss von Temperatur-Unterschieden und Rotations-Impulsen. *Z. Meteor.*, **1**, 227–230.

White, A. A. (1986). Documentation of the finite difference schemes used by the Met O 21 2D Navier-Stokes model. Technical report, Geophysical Fluid Dynamics Laboratory, UK Meteorological Office. Internal Report Met O 21 IR86/3.

Williams, G. P. (1979). Planetary circulations: 2. The Jovian quasi-geostrophic regime. *J. Atmos. Sci.*, **36**, 932–968.

Williams, P. D. (2003). *Nonlinear interactions of fast and slow modes in rotating, stratified fluid flows*. Ph.D. thesis, Oxford University.

Williams, P. D., Read, P. L., & Haine, T. W. N. (2003). Spontaneous generation and impact of inertia-gravity waves in a stratified, two-layer shear flow. *Geophys. Res. Lett.*, **30**(24), 2255.

Yoshida, A. & Hart, J. E. (1986). A numerical study of baroclinic chaos. *Geophys. Astrophys. Fluid Dyn.*, **37**, 1–56.